MDPI

Article

Shoreline Evolution and Erosion Vulnerability Assessment along the Central Adriatic Coast with the Contribution of UAV Beach Monitoring

Gianluigi Di Paola [1,2], **Antonio Minervino Amodio** [3,*], **Grazia Dilauro** [1], **Germàn Rodriguez** [4,5] **and Carmen M. Rosskopf** [1]

1   Department of Biosciences and Territory, University of Molise, Contrada Fonte Lappone, I-86090 Pesche, Italy
2   Department of Biological, Geological, and Environmental Sciences, University of Bologna "Alma Mater Studiorum", Via Zamboni 67, I-40126 Bologna, Italy
3   National Research Council (CNR), Institute of Heritage Science (ISPC), I-00185 Tito, Italy
4   Departamento de Física, Universidad de Las Palmas de Gran Canaria, 35001 Las Palmas de Gran Canaria, Spain
5   Institute of Environmental Studies and Natural Resources (iUNAT), Universidad de Las Palmas de Gran Canaria, 35001 Las Palmas de Gran Canaria, Spain
*   Correspondence: antonio.minervinoamodio@ispc.cnr.it; Tel.: +39-0971-427-309

Abstract: Coastal erosion and its impacts on the involved communities is a topic of great scientific interest that also reflects the need for modern as well as cost and time-effective methodologies to be integrated into or even to substitute traditional investigation methods. The present study is based on an integrated approach that involves the use of data derived from UAV (Unmanned Aerial Vehicle) surveys. The study illustrates the long- to short-term shoreline evolution of the Molise coast (southern Italy) and then focuses on two selected beach stretches (Petacciato and Campomarino beaches), for which annual UAV surveys were performed from 2019 to 2021, to assess their most recent shoreline and morpho-topographical changes and related effects on their coastal vulnerability. UAV data were processed using the Structure from Motion (SfM) image processing tool. Along the beach profiles derived from the produced DEMs, the coastal vulnerability of the selected beach stretches was evaluated by using the Coastal Vulnerability Assessment (CVA) approach. The results obtained highlight some significant worsening of CVA indexes from 2019 to 2021, especially for the Campomarino beach, confirming the importance of the periodic updating of previous data. In conclusion, the easy use of the UAV technology and the good quality of the derived data make it an excellent approach for integration into traditional methodologies for the assessment of short-term shoreline and beach changes as well as for monitoring coastal vulnerability.

Keywords: shoreline evolution; beach erosion; UAV data elaboration; coastal vulnerability assessment; CVA approach; Molise coast; Italy

1. Introduction

Coasts are dynamic systems that change in form at different space and time scales in response to geomorphological and marine forces [1–3]. Coastal landforms, affected by short-term perturbations such as storms, frequently return to their pre-disturbance morphology, thus reflecting a basic, morphodynamic equilibrium [4]. Most coasts are constantly adjusting towards a dynamic equilibrium, frequently adopting different 'states' in response to variable wave energy and sediment supply [5]. Coasts exhibit natural variability in response to changes in environmental factors, which can make it difficult to identify the impact of climate change. Thus, for instance, most beaches across the world show evidence of recent erosion, but ongoing sea-level rise is not always considered to be the major cause. Erosion can result from several other factors, both natural and

anthropogenic, such as reduced fluvial sediment input [6], offshore bathymetric changes [7], altered wind and wave patterns [8,9], or a mix of factors [10].

The assessment of coastal erosion and flooding is an important issue for the scientific community, considering that a significant and increasing share of the world population currently lives in coastal areas. In fact, the United Nations, during the Ocean Conference 2017 [11], highlighted that more than 10% of the world population (600 million people) live along coastal areas that are less than 10 m above sea level, while about 40% of the world population (2.4 billion people) live within 100 km from the coastline. Moreover, the possible increase of seal level could force the displacement of up to 187 million people globally during this century [12]. As for the Italian peninsula, which has approximately 7500 km of coastline, the data released by the Ministry of Environment, Land, and Sea Protection [13] for the period of 1960–2012 show that 23% (1534 km) of this coastline has experienced erosion, resulting in a total land loss of 35.5 km^2.

Assessing coastal evolution and recent erosion trends along with related natural and/or anthropogenic causes is crucial for the correct definition of near-future planning and interventions aimed at combatting erosion and ensuring the sustainable development of coastal zones.

To this end, an appropriate experimental observation of coastal zones with their complex and variable dynamics and configurations is of paramount importance. In this regard, traditional methods suitable for measuring, mapping, and monitoring beach–dune systems and shoreline changes are commonly applied, such as the interpretation of topographic maps and aerial images. Related activities, however, take a long time and immense effort to complete, and they may not provide the necessary spatial scale and local details and/or comprehensively cover the most recent time intervals [14]. Fortunately, such limitations in spatio-temporal resolution are now being overcome, or at least alleviated, thanks to the access to large satellite databases and the development of various technologies appropriate for this purpose. In particular, the progress and easy accessibility of Unmanned Aerial Vehicle (UAV) technology has enabled the development of an alternative coastal monitoring technique that efficiently captures spatial and temporal requirements across a wide range of environmental applications [15–19], with the important added advantage of making the task much less tedious.

This study presents an integrated approach involving traditional methods and the innovative UAV methodology to study the shoreline evolution and morphodynamic behaviour of the Molise coast, a well-known coastal system that has been under continuous study for some decades and one of the most vulnerable coastal regions in Italy (e.g., see [20–22] and references therein).

The major aims of this study are: (i) to assess the spatial-temporal distribution of shoreline changes that occurred along the Molise coast from 1954 to 2016 using remotely sensed data and topographic maps; (ii) to assess long- to short-term shoreline changes of two selected test areas and, by means of UAV-derived data, their most recent shoreline and morpho-topographic beach–dune changes, and (iii) to assess the possible influence of such changes on the vulnerability of the test areas to coastal erosion and inundation.

2. The Molise Coast

2.1. Physiographic and Geomorphological Features

The coastline of the Molise region (Figure 1) is approximately 36 km long and part of the Central Italian Adriatic coast. Its northern and southern boundaries are respectively the Formale del Molino channel and the Saccione Stream (Figure 1). A major part of the Molise coastline (22 km) consists in a low sedimentary coast with sandy beaches, while its central sector (ca. 14 km long) consists in a high rocky coast. The latter was formed by Plio-Pleistocene sedimentary successions composed of clayey-sandy marine and sandy-conglomeratic fluvial sediments (Montesecco Clay, Serracapriola Sand, and Campomarino Conglomerate formations) [23]. The sea cliffs are cut into the Plio-Pleistocene bedrock and are mostly inactive and set back from the shoreline, with the only exception of the short

but artificially protected cliff of the Termoli promontory [21]. Consequently, the beaches are practically continuous along the entire Molise coast, leaving aside the interruptions owing to the major river mouths (Trigno and Biferno rivers and Sinarca and Saccione streams, Figure 1) and the three harbours present along the coast (Figure 1). The beaches are largely made up of fine to medium-grained sands and characterized by very variable widths ranging between a few meters and 93 m [21]. The dominant longshore transport occurs from NW to SE [10,21].
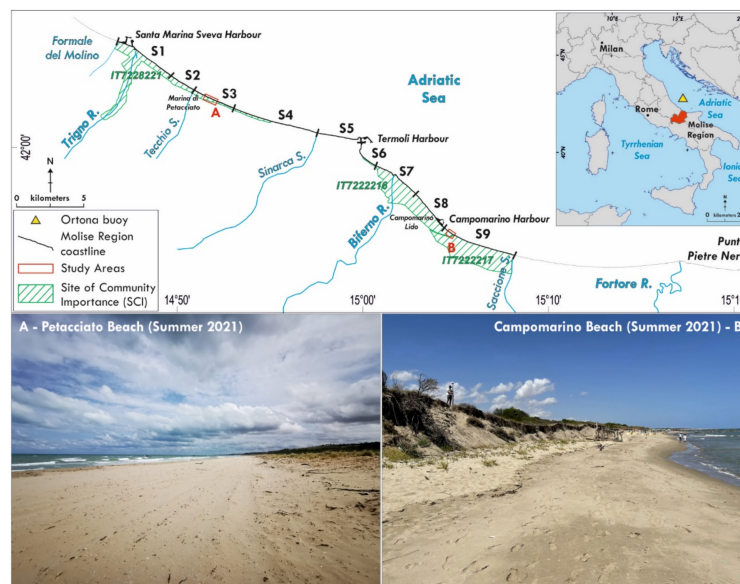

Figure 1. The Molise coast. Location and panoramic views of the two study areas, A and B.

The Termoli promontory divides the Molise coast into two nearly independent sectors (physiographic sub-units) [21]. These sectors, hereinafter named the northern and southern Molise coasts, are oriented in the WNW and NW-SE directions, respectively.

The Molise coast has an important ecological value thanks to the presence of 18 habitats of interest for the European Community [24,25]. In particular, there are three Sites of Community Importance (Figure 1), which include the three major river mouths (Trigno, Biferno, and Saccione) from north to south: IT7228221 (Foce Trigno-Marina di Petacciato), where test area A is located, IT7222216 (Foce Biferno-Litorale di Campomarino), which includes test area B, and IT7222217 (Foce Saccione-Bonifica Ramitelli). Habitats of community interest with a high naturalistic value cover an area of more than 340 hectares [25], highlighting the fact that the Molise coastline is one of the most important natural coastal stretches along the Italian Adriatic coast.

Concerning the reconstruction of the evolution of the Molise shoreline, in agreement with previous studies (e.g., see [21] and references therein), the subdivision in nine coastal segments (S1–S9, Figure 1) has been maintained to allow for an easy comparison of the shoreline change data calculated in the present study and those calculated previously.

Literature data (e.g., [21] and references therein) show that erosion strongly controlled the long-term evolution of the Molise coast. The coastal segments that include the Trigno and Biferno river mouths (S1 and S7) suffered important shoreline retreat (Figure 2), totalling average annual rates of −2.7 m/y and −2.9 m/y, respectively, during the period of 1954–2014 [21]. On the other hand, segments S2, S4, S5, S8, and S9 remained substantially stable (0.1 m/y–0.3 m/y), while S3 and S6 even experienced some slight advance (0.8 m/y and 1.0 m/y, respectively). Shoreline erosion was driven in particular by the decrease of fluvial sediment input to the coast, mostly resulting from in-channel mining and hydraulic interventions at the basin and from the fluvial reach scale from the 1950s onwards (e.g., [10,21] and references therein). To face the ongoing coastal erosion, numerous defence structures were built from the 1980s onwards, mostly under emergency conditions, allow-

ing for the partial balancing out of previous erosion trends (for example, see S5 in [21]). In fact, hard defence structures (adherent breakwaters, emerged and submerged detached breakwaters, revetments, groins, and jetties) cover about 62% of the Molise coast [21]. Despite a relatively high degree of coastal protection as early as 1998, erosion continued to significantly affect the Molise coast [21]. Especially during very recent years (the period of 2011–2014), shoreline erosion not only involved segments S1 and S7 but also extended to segments S2, S3, and S9 (−4.9 m/y, −3.3 m/y, and −3.6 m/y, respectively), suggesting an ongoing process of progressive shoreline destabilization [21].
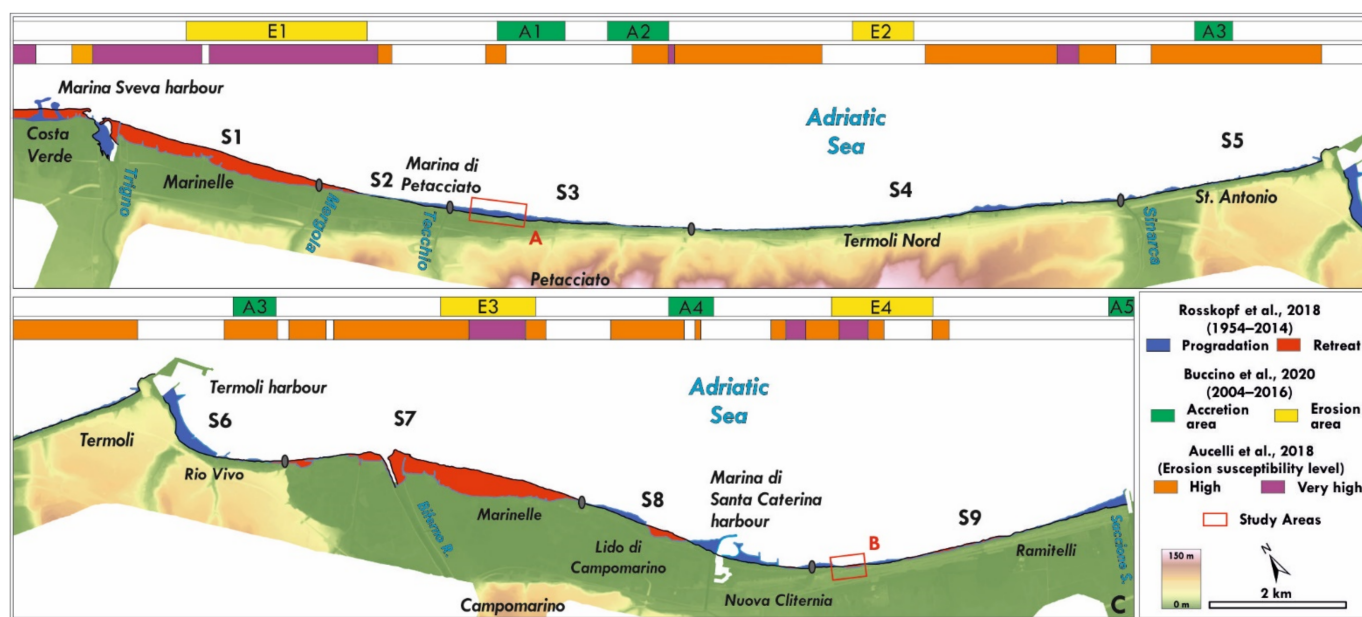

Figure 2. Shoreline progradation and retreat rates from 1954 to 2014 [21], location of areas with high to very high levels of erosion susceptibility [22], and location of mid-term (2004–2016) major shoreline erosion/accretion areas E1–E4 and A1–A5 [10].

Recent data provided by Buccino et al. 2020 [10] on the evolution of the Molise shoreline from 2004 to 2016 (Figure 2) highlight the presence of two major erosion areas located south of the Trigno and Biferno river mouths (E1 and E3), and of two others (E2 and E4) falling within coastal segments S4 and S8, respectively. Furthermore, the study shows the presence of several major accretion areas (A1–A5), which are characterized by a positive sediment balance.

Finally, the data reported by Aucelli et al. (2018) [22] show that most of the Molise shoreline is characterized by a high level of erosion susceptibility, while nearly the entire segment S1 and smaller portions of S4, S7, S8, and S9 are characterized by a very high susceptibility level (Figure 2).

2.2. Meteomarine Features of the Molise Coast

Wind, wind-generated waves, and astronomically and meteorologically induced sea level variations affecting the Molise coast are framed in the meteo-marine context that characterizes the Adriatic Sea.

Typical strong winds above the Adriatic Sea are generally of two types, Bora and Sirocco. Apart from these, any other class of windstorms has negligible importance regarding wave storms, both in frequency and intensity [26]. Sirocco is a humid, warm, and steady wind blowing over the Adriatic basin from SE-SSE. This wind is strongly influenced by the orography as it is channelled along the major axis of the basin by the Apennines and the Dynaric Alps. It blows on most of the length of the basin, usually not very strong, but is able to produce storms in the Central and Northern Adriatic areas [26]. On the other hand, Bora is a cold and gusty, strong, low-level, downslope wind blowing mainly from

NE, across the mountain barrier of the Dinaric Alps. Strong bora events may give rise to structured jets and multiple jet systems flowing through orographic gaps, with strong sub-basin scale spatial gradients across the Adriatic [27,28].

Because of the meteorological scenario above, wave climate in the Adriatic Sea is usually mild or moderate most of the year. However, the severity of wave climate varies throughout the basin depending on the relative importance of the dominant and prevailing winds, Bora and Sirocco, as well as on the fetch available for generating waves. In general, Bora is more intense than Sirocco and is fetch-limited, blowing mainly along the minor axis of the Adriatic, although it can suddenly attain very high speeds. On the contrary, Sirocco may blow over much larger fetches, along the major axis of the basin, and may grow slowly. Furthermore, Sirocco generally reaches the highest speeds in the eastern Adriatic regions and decreases while proceeding to the western coasts [27]. In particular, wind fields in the Central Adriatic Sea are strongly conditioned by the bordering orography, with the wind channelled along the main axis and with the presence of a reduced but still important effect of the transverse component.

In line with these, coastal topography and geometry also significantly influence wave generation by Bora and Sirocco in the Central Adriatic Sea. In particular, wave climate in the Central Western Adriatic Sea is conditioned by the presence of the Conero and Gargano headlands at its northern and southern limits, which significantly restrict the fetch in the longitudinal direction. Accordingly, potential fetches for the study area are larger along sectors oriented around the N and E directions and decrease towards the NE.

Given these wind conditions, waves approaching the Molise coast exhibit a bimodal directional distribution, with two prevailing directional sectors. One of these sectors is roughly represented by the directional quadrant between the NW and the NE, hereinafter referred to as the main wave direction, while the second directional sector extends from the NE to the SE, and is referred to as the secondary wave direction (Table 1). Wave fields approaching from the NE-SE sector are characterized by low and moderate significant wave heights, $H_s < 3$ m, and with the largest percentage of observations corresponding to events with $H_s < 1$ m. The contribution of low and moderate sea states also prevails in the NW-NE directional sector. However, in this case, the sea states may be more severe, with H_s values of more than 3 m and up to 6 m, although the frequency of these events is notably low. Nevertheless, the bimodal character of the bivariate distribution of H_s and wave direction becomes clearly unimodal and oriented mainly around the NNE sub-sector for sea states with $H_s > 3$ m [21]. In this sense, an analysis of the annual maximum significant wave height at the Ortona buoy (Sea Wave Measurement Network, RON) in the period of 1990–2006 reveals that this parameter ranges from 3 to 6 m, approaching from the N-NE directional sector, although the most severe events arrive from the N-NNE sub-sector (Figure 3A). The occurrence of these extreme episodes takes place during the late autumn, winter, and early spring months (Figure 3B). The main wave climate features of the Molise coast, including the Average Significant Wave Height (H_s) and the Average Significant Wave Height of sea states exceeding 2 m (H_t), as well as their associated periods, are reported in Table 1.

Table 1. Main wave climate features estimated for the Molise coast. Average Significant Wave Height (H_s) and the associated period (T_s); Average Significant Wave Height of events exceeding 2 m (H_t) and the corresponding period (T_t).

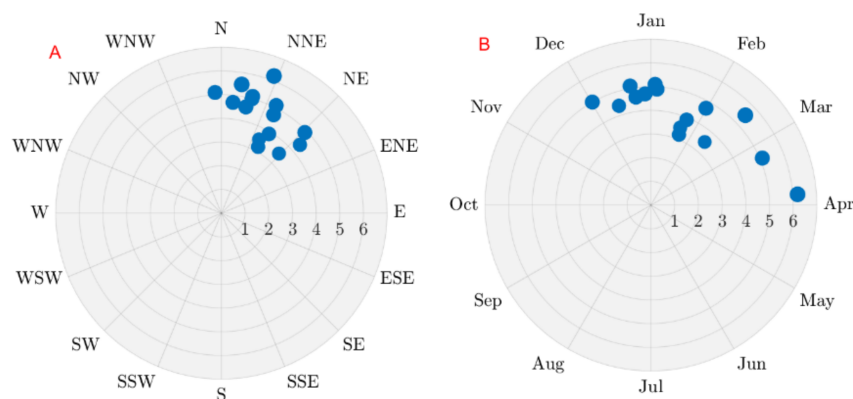| Recording Period (Ortona Buoy)	Main Wave Direction (°N)	Secondary Wave Direction (°N)	Effective Fetch (km)	H_s (m)	T_s (s)	H_t (m)	T_t (s)
1990–2006	340–10	70–100	476	0.7	3.5	3.5	6.6

Figure 3. Annual maximum wave storms, directionality (**A**) and timing during the year (**B**) at the Ortona buoy (1999–2006). For the location of the Ortona buoy, see Figure 1.

In correspondence with the directions of the prevailing and dominant waves and the shoreline orientation of the Molise coast, longshore drift occurs in the north–south direction [21,29,30].

Regarding astronomical tides, the study area is microtidal and experiences ordinary tidal excursions of 30–40 cm [21], although the maximum high tide recorded in the tide tables is 0.6 m and the minimum height is –0.2 m, which are referenced to mean lower low water [31]. Sea-level oscillations induced by meteorological conditions (storm surges or meteorological residues) are obtained as the difference between the measured sea level and the predicted astronomical tide. Analyses of meteorological residues obtained from sea level measurements at the Ortona tidal gauge [32] for the period between 1979 and 2019 indicate that storm surge values range approximately between −0.15 m and 0.45 m. Nevertheless, more than 95% of the observations lie in the range of −0.07 m–0.27 m, and the probability of the occurrence of values greater than 0.3 m are less than 0.01.

2.3. The Test Areas

To assess the most recent shoreline changes with the use of UAV-derived data, we selected two test areas (A and B, Figures 1 and 2). These test areas allowed us to investigate two different situations: one concerning conditions of essential stability for both the shoreline and the beach–dune system, and the other relating to evident erosion and destabilization, either recent or perhaps ongoing, which involve previously stable coastal segments.

Test area A falls under segment S3 (northern Molise coast, Figure 2) and is part of the Petacciato coastline. It consists in a 400 m long stretch of coast located 500 m south of Marina di Petacciato. This area is characterized by a sandy beach about 30 m wide, supported by a well-preserved dune system that is wider than 10 m and up to 4 m high.

Test area B is located along the southern Molise coast in the northernmost part of segment 9 (Figure 2), at approximately 1.5 km south of the Campomarino touristic port, and is part of erosion area E4, indicated by Buccino et al. (2020) [10]. It consists in an approximately 200 m long coastal stretch that is characterized by a 6–25 m wide sandy beach and an up to 4 m high dune system, whose original dune front has been replaced by a sub-vertical erosion scarp up to 2.5 m high that clearly separates the dune from the backshore. In front of test area B, 160–200 m from the shoreline, there are three breakwaters. They belong to a row of nine (originally) emerged and detached breakwaters approximately 700 m long, oriented slightly obliquely to the coast, and placed between 2001 and 2005. Furthermore, in front of the central part of area B, a detached groin (placed in 2011–2014) is located approximately 30 m from the shoreline (for further details, see Section 4.2).

3. Materials and Methods

This section describes the materials and methods used to investigate the long to short-term evolution of the Molise coast, the short-term morpho-topographical changes of the test areas from 2019 to 2021, and the possible impact of such changes on the coastal vulnerability assessment.

3.1. Evaluation of Shoreline Changes through the DSAS Tool

The digitization of the Molise shorelines was carried out in the ArcGIS environment using aerial photos from 1954, orthophoto maps from 2004, and images taken by Google Earth in 2016 (Table 2).

Table 2. Data sources used to calculate the shoreline variations in the test areas. RMSE = root mean square error.

Date	Data Source	Scale	RMSE (m)
1954	Aerial photo	1:36,000	5
2004	Orthophoto map	1:2500	3
2016	Google Earth image	1:500	1

Regarding the shorelines of the test areas in 2019, 2020, and 2021, we used the orthophoto images realized by the UAV surveys performed during this study, as shown below. As the test areas are part of a microtidal environment, the shoreline positions were defined as the water line at the time of the photo [33], but a maximum uncertainty of ± 1.6 m was assumed for the daily water line position, as it was not possible to reconstruct the tidal conditions for each image.

To evaluate shoreline changes, we used the Digital Shoreline Analysis System (DSAS), a freely available extension to ESRI's ArcGIS [34]. This tool, which automatically creates regularly spaced transects, provides two parameters. First, a distance parameter (Net Shoreline Movement—NSM) that measures the distance between the oldest and the youngest shoreline considered for each transect, and second, the Linear Regression Rate (LRR), which represents the average rate of accretion or erosion obtained after fitting a least-square straight line to each shoreline section, for each considered period. In detail, shoreline variations were determined for the Molise coast by using 352 transects placed at an equidistance of 100 m. As we needed a lot more details for the test areas, we fixed an equidistance value of 5 m.

3.2. Monitoring of Morpho-Topographic Changes in the Test Areas Based on UAV-Derived Data

The monitoring of the short-term evolution of the test areas was based on annual UAV surveys. To date, three UAV survey campaigns have been carried out—in July 2019, 2020, and 2021; a Phantom 3 Standard (Quadcopter) was used, which is a drone developed by Da-Jiang Innovations (DJI, Shenzhen, China). This drone was mounted with a stabilized camera that compensated for involuntary movements of the UAV due to wind, thus ensuring the correct orientation of the photos with respect to the ground. The coordinates for each photo were then registered by an internal GPS, allowing the drone to follow the points (waypoints) previously fixed with the GPS on the flight plan. An average flight altitude of 40 m was used for all surveys, which allowed for a ground resolution of 1.5 cm/px. Using the default camera of the Phantom 3 Standard, about 250 images with a longitudinal overlap (flight direction) of 85% and a flight strip overlap of 60% were obtained during each flight.

For all flights, six targets, 40×40 cm in size and easily visible from above, were placed to record the position of the Ground Control Points (GCPs) and consequently to orient the model in space. A GNSS receiver in static nRTK mode was used to acquire the GCPs.

To evaluate the variations in the plano-altimetric features of the test areas and the related volumetric changes, 3D models were generated. To obtain these models, the (2D) photos acquired with the drone were processed using the Structure from Motion (SfM)

algorithm, which internally implements the photogrammetry and computer vision methods. A functional correlation between the 3D object points and the 2D image points via the collinearity condition is the core concept behind photogrammetric image data processing [35]. The examination of two photos and related orientation parameters allowed for the identification of the common points and the determination of the related 3D coordinates.

To obtain the final outputs (Dense Cloud Points, DEMs, and orthophotos), we proceeded as follows: (i) generation of the flight plan; (ii) field work consisting in the positioning of the targets, measurement of the position with the GNSS receiver, and acquisition of photos with the UAV; (iii) aerial data processing (as described by Snavely et al. (2008)) [36], error checking of the model against GCPs, and export of point clouds, DEMs, and orthophotos.

Minervino Amodio et al. (2022) [14] already highlighted that there is a strong correlation between the points surveyed on the beach with the GNSS and the UAV techniques. This correlation allowed us to directly use the DEMs 2019, 2020, and 2021 obtained from the UAV surveys for extracting the beach profiles needed for our investigation. Overall, 12 beach profiles, extending from the top of the dune ridge up to the water line (see below), were extracted.

3.3. Coastal Vulnerability Assessment

The vulnerability to coastal erosion and inundation was evaluated for the test areas by means of the Coastal Vulnerability Assessment (CVA), a method developed by Di Paola et al. (2014) [37], starting from the preliminary approach used for the coastal vulnerability assessment of several coastal areas [37–40]. For the vulnerability evaluation, the CVA method allowed us to consider both the beach retreat due to storm surges (using wave climate and geomorphological data such as bathymetry, beach sedimentology, and beach width) and the coastal inundation due to run-up on the beach. To this aim, morpho-sedimentary beach features, wave climate, and multi-temporal series of aerial photographs and topographic maps were analysed.

In detail, the CVA method evaluates the coastal vulnerability for each considered period according to the following equation:

$$CVA = I_{Ru} + I_R + E + T_i \qquad (1)$$

where I_{Ru} is the wave run-up height index, which is given by the run-up level divided by the beach foreshore slope [41]; I_R is the short-term erosion index, which provides a measurement of the maximum beach recession due to storms, normalized with the beach width [42]; E is the beach erosion rate in m/y, and T_i measures the horizontal distance travelled by the tidal range. In this work, $T_i = 0$, because the Molise coast is microtidal and experiences ordinary tidal excursions of 30–40 cm [21].

The I_{Ru} index provides the measurement of the potential inundation capacity that characterizes natural beaches during wave storms. According to Stockdon et al. [41], the wave run-up height is provided by $Ru_{2\%}$, i.e., the wave run-up level exceeded by 2% of the number of incoming waves, which is measured vertically from the still water line. This value is projected along the beach through the calculation of $X_{Ru2\%}$, which corresponds to the horizontal distance travelled by the wave in the run-up process. Therefore, I_{Ru} takes on values that depend on the percentage associated with the maximum horizontal run-up distance of the wave on the beach ($X_{Ru2\%}$), which is normalized with respect to the width of the emerged beach (L). In this way, the I_{Ru} index can be customarily clustered into four discrete levels, as shown in Table 3.

Table 3. Coastal vulnerability assessment (CVA) classification scheme (according to [37]).

Variable	1	2	3	4
I_R (%)	≤ 15	16–30	31–50	>50
I_{Ru} (%)	≤ 40	41–60	61–80	>80
E (m/y)	≥ -0.5	-0.6–-1.0	-1.1–-2.0	<-2.0
	Low	**Medium**	**High**	**Very High**
CVA	$\leq$**6**	**7–9**	**10–12**	$\geq$**13**

The I_R index instead provides the measurement of the potential beach retreat and is used for the dynamical calculation of the shoreline retreat based on the convolution method of Kriebel and Dean (1993) [42]. I_R values depend on the percentage associated with the maximum beach retreat (R_{max}), normalized with the beach width L. As a result, I_R values depend on the percentage associated with R_{max}, normalized with respect to the width of L. In addition, the I_{Ru} and I_R indexes can be customarily clustered into four discrete levels (Table 3).

Considering that the evolution of a beach is not only linked to the effects produced by coastal inundation during extreme events (H_t = 3.5 m, Table 1) but also to those caused by ordinary wave dynamics (H_s = 0.7 m, Table 1), the parameters I_{Ru} and I_R were calibrated considering both conditions, using Formula (2) and (3), respectively.

$$I_{Ru} = \left(I_{Ru\ (H_s)} + 2 \cdot I_{Ru\ (H_t)} \right)/3 \tag{2}$$

$$I_R = \left(I_{R\ (H_s)} + 2 \cdot I_{R\ (H_t)} \right)/3 \tag{3}$$

Regarding the E index, the evolution of the shoreline in the mid-term (periods 1954–2004 (E_1) and 2004–2016 (E_2)) and the short term (periods 2016–2019 (E_{2019}), 2016–2020 (E_{2020}), and 2016–2021 (E_{2021})) were considered. To this aim, we used the indications proposed by Cromwell [43], following Equation (4).

$$E = (E_1 + 2 \cdot E_2 + 3 \cdot E_{2019/2020/2021})/6 \tag{4}$$

The E index can be customarily clustered into four discrete levels (Table 3).

4. Results

4.1. Long- and Mid-Term Shoreline Changes along the Molise Coast from 1954 to 2016

The application of the DSAS method allowed for the calculation of the long and mid-term shoreline changes of the Molise coast (see northern and southern Molise coast, Figures 4 and 5) for the periods of 1954–2004, 2004–2016, and 1954–2016 (Table 4).
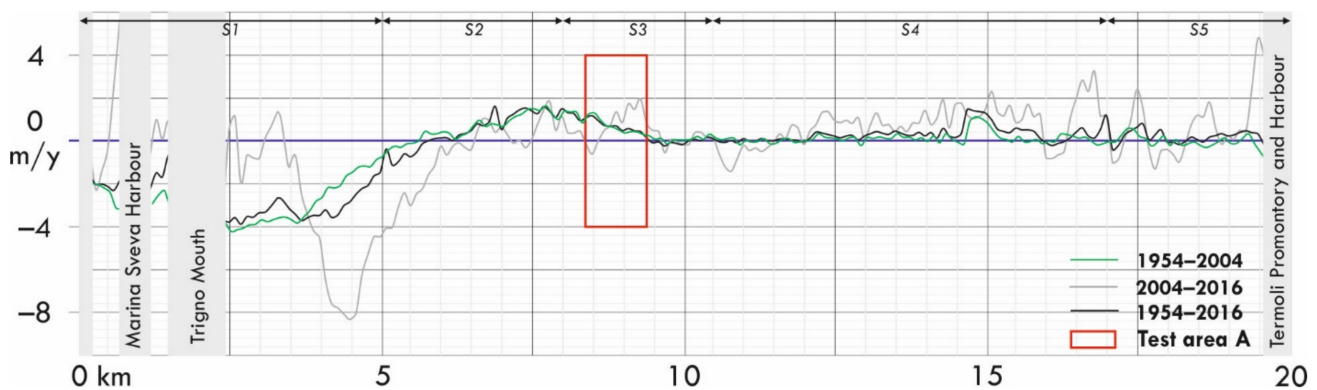

Figure 4. Long- to mid-term annual shoreline changes along the northern Molise coast (segments S1–S5) during the periods 1954–2016, 1954–2004, and 2004–2016.
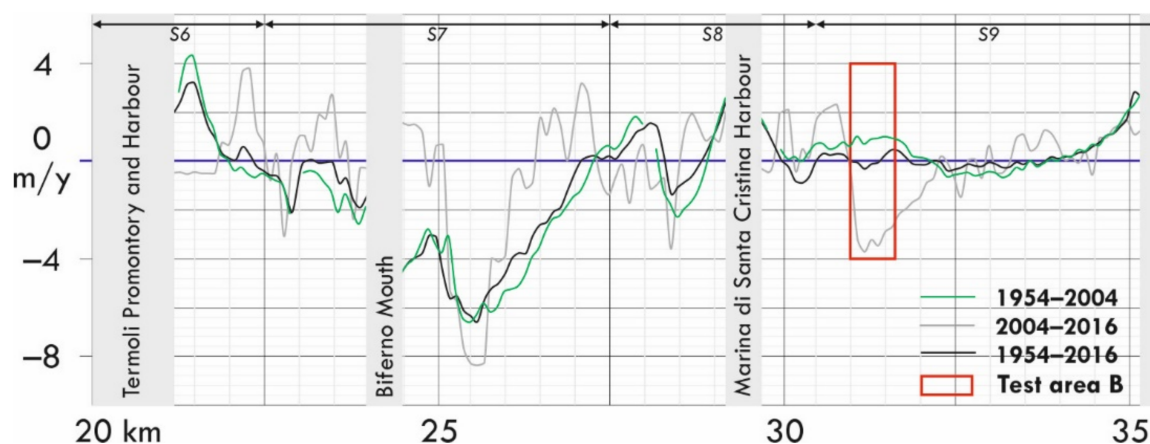
Figure 5. Long to mid-term annual shoreline changes along the southern Molise coast (segments S6–S9) during the periods 1954–2016, 1954–2004, and 2004–2016.

Table 4. Long and mid-term shoreline changes along the Molise coast.

Segment	1954–2016		1954–2004		2004–2016	
	NSM (m)	LRR (m/y)	NSM (m)	LRR (m/y)	NSM (m)	LRR (m/y)
S1	−132.5	−2.2	−142.1	−2.6	−26.1	−2.1
S2	−6.9	0.1	6.2	0.3	−13.1	−1.2
S3	33.9	0.7	27.5	0.7	6.4	0.5
S4	15.0	0.3	7.2	0.1	7.9	0.7
S5	4.8	0.2	−1.9	−0.1	6.7	0.7
S6	60.9	1.1	49.9	1.0	9.1	0.8
S7	−172.0	−2.7	−169.8	−3.4	−14.0	−1.2
S8	23.4	0.3	26.7	0.5	3.7	0.3
S9	9.4	0.3	9.8	0.2	−5.7	−0.5

Regarding the long-term evolution of the Molise coastline (time interval, 1954–2016), the results obtained (Figures 4 and 5, Table 4) confirm that erosion mainly affected segments S1 and S7, which underwent an overall average shoreline retreat of −132.5 m and −172.0 m, respectively (Table 4). Minor erosion areas are present in the northern part of S2, in the central and southernmost parts of S8, as well as in the northern portion of S9. However, segments S3, S4, S6, and S8 show an overall positive balance, and segments S2, S5, and S9 demonstrate substantial stability.

Shoreline changes calculated for the period of 1954–2004 obviously largely confirm this general trend, but these indicate major erosion rates for segments S1 and S7 (LRR of −2.6 m/y and −3.4 m/y, respectively; Table 4) with respect to the period of 1954–2016, thus highlighting a more intense shoreline erosion in these segments during the first 50 years of the considered time interval.

With reference to shoreline changes from 2004 to 2016, data highlight some trend inversions with respect to previous shoreline changes, from negative to positive and vice versa, which affect, for example, the northern part of S1, some parts of segments S6 and S7, as well as the two test areas. Shoreline retreat persists in segment S1, similar to the previous period (LRR of −2.1 m/y, Table 4), while the annual rates of S7 evidence a clear trend towards conditions of minor erosion (LRR of −1.2 m/y, Table 4). Furthermore, segments S2 and S9 show an overall trend towards moderate and slight shoreline retreat, respectively (LRR of −1.2 m/y and −0.5 m/y, respectively; Table 4), while the other coastal segments—and therefore also S3, where test area A is located—show an overall stability.

4.2. Morpho-Topographic Changes of the Beach–Dune Systems in the Test Areas from 2019 to 2021

Based on the data acquired during the UAV flights in 2019, 2020, and 2021, we produced the orthophotos and the related DEMs for test areas A and B, illustrated in Figures 6 and 7.

Figure 6. Orthophotos and DEM hillshades produced with the data acquired during the UAV flights in 2019 (**A**,**D**), 2020 (**B**,**E**), and 2021 (**C**,**F**) along Petacciato beach. (**A**) shows the locations of beach profiles P1–P7 extracted from the DEMs.
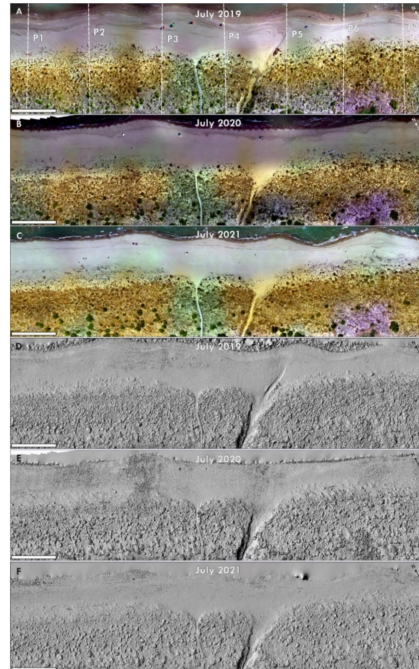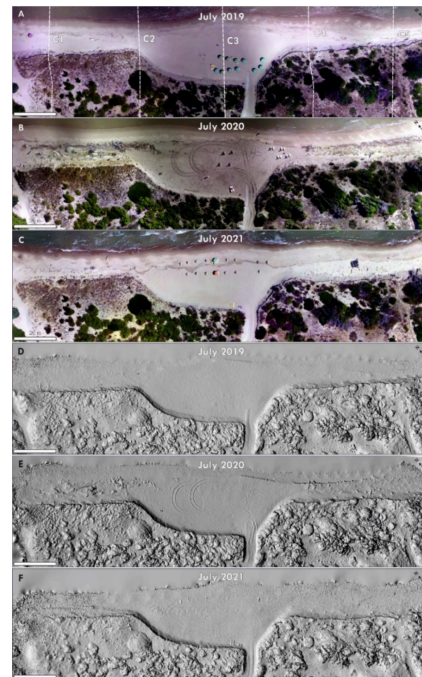

Figure 7. Orthophotos and DEM hillshades produced with the data acquired during the UAV flights in 2019 (**A**,**D**), 2020 (**B**,**E**), and 2021 (**C**,**F**) along Campomarino beach. (A) shows the locations of beach profiles C1–C5 extracted from the DEMs.

A comparison of the orthophotos and DEMs produced for test area A (Petacciato beach, Figure 6) gives evidence of the substantial stability of the dune vegetation cover and the variable coverage of vegetation debris on the beach. Slight shoreline movements are evidenced by small shoreline undulations varying from year to year, suggesting the probable role of longshore drift in local beach nourishment and erosion.

Comparing the orthophotos and DEMs obtained for test area B (Campomarino beach, Figure 7) highlights significant differences as to the morpho-topographic and vegetational features of its beach–dune system, allowing for the identification of a northern, southern, and central portion. The latter, in particular, is characterized by a larger beach and a dune front localised in a more internal position, approximately 15 m with respect to the adjacent beach portions. The comparison of recent Google Earth pictures (Figure 8) shows that the entire shoreline of test area B has undergone a more or less consistent retreat between June 2016 and July 2019 (up to approximately 30 m) despite the presence of the three breakwaters in front (but almost completely submerged, at least since 2014; Figure 8) and a groin, which was definitely detached in this period.

Figure 8. Evidence of shoreline and beach changes from 2016 to 2019 (Google Earth images dating back to 20 June 2016 and 20 July 2019) along the coastal stretch that includes test area B. On the Google Earth image from 2019, the white line indicates the shoreline of 2016.

Despite the fact that the entire shoreline of test area B has retreated from 2016 and 2019, the northern and southern sectors have not undergone a similar dune front retreat. This consideration, together with other observations (see below), led us to believe that the dune retreat in the central sector was not due to natural erosion but to human interventions aimed at enlarging the beach and also recovering, in this way, a part of the beach lost due to the shoreline retreat between June 2016 and July 2019 (Figure 8). In fact, this beach sector is used by the Marinelle campsite for bathing, as shown in several google earth images by the

presence of beach umbrellas and pedestrian access that cuts through the dunes, connecting the campsite directly with the beach. The latter appears clean, without vegetation debris, while the presence of several excavator footprints in the images of 2020 (Figure 7B,E), along with direct observations in the field, confirm periodic operations of cleaning, levelling, and enlargement of the beach in the pre-summer period.

For all beach profiles surveyed in the test areas in 2019, 2020, and 2021 (for location, see Figures 6A and 7A), the major morphometric features were determined.

Table 5 illustrates the major morphometric features of the beach profiles surveyed in 2019 and 2021.

Table 5. Comparison of main morphometric features of beach profiles in 2019 and 2021.

Profiles	Backshore Width—L (m)		Backshore Slope—β_b (%)		Foreshore Slope—β_f (%)		Total Slope—m_o (%)		Berm—B (m)		Dune Front Retreat (m)	D_{50} (mm)
	2019	2021	2019	2021	2019	2021	2019	2021	2019	2021	-	-
P1	34.1	30.7	3.7	1.1	5.7	6.0	4.0	2.9	0.3	0.5	-	
P2	28.8	21.9	2.7	2.2	25.4	8.4	6.2	3.6	1.4	0.4	-	
P3	27.9	20.4	2.8	2.4	21.8	10.8	6.5	4.8	1.4	0.8	-	
P4	28.5	24.4	6.2	4.1	14.2	10.0	8.1	5.4	1.1	0.8	-	0.47
P5	23.9	20.5	4.7	5.3	8.0	6.4	5.7	5.6	0.8	0.5	-	
P6	22.5	21.2	6.7	4.5	17.5	8.7	10.3	5.9	1.1	0.6	-	
P7	18.9	16.5	4.0	5.6	13.1	6.8	6.3	6.0	0.7	0.5	-	
C1	10.5	8.4	9.8	15.6	8.6	18.2	9.3	22.2	0.6	0.3	0.4	
C2	9.2	7.5	9.4	22.8	10.9	10.1	10.0	17.5	0.5	0.6	1.2	
C3	24.1	20.0	4.2	4.8	10.0	5.3	5.1	5.0	0.5	0.6	0.4	0.50
C4	6.8	6.1	8.9	19.8	14.9	5.3	10.6	11.3	0.5	0.5	2.1	
C5	4.9	5.9	15.8	6.0	3.5	10.3	9.5	8.2	0.2	0.6	1.5	

Test Area A

Comparing data obtained for profiles P1–P7 (Table 5) for 2019 and 2021 highlights the following trends: A slight restriction of the backshore width, and aside from a few exceptions, the decrease of backshore, foreshore, and total slopes as well as a slight decrease in the height of the ordinary berm. However, no dune front retreat occurred along these profiles from 2019 to 2021.

Test Area B

Comparing data obtained for profiles C1–C5 highlights the following trends: A slight restriction of the backshore as well as partial increases and decreases of the backshore and foreshore slopes, which resulted in an overall increase of the total beach slopes along C1 and C2 from 2019 to 2021 and their substantial stability along C3–C5. In addition, berm heights alternately increased or decreased. Finally, all profiles showed some dune front retreat, between 0.4 and 2.1 m.

Figure 9 illustrates the short-term evolution of beach profiles P6 and C4 from 2019 to 2021. These profiles, indicated by Rosskopf et al. (2018) [21] as profiles P1 and P2, respectively, have already been under study for two decades and were surveyed in 2001, 2010, and 2016. Hence, they are taken as a reference for the overall evolution of the beach–dune systems in the test areas in the last two decades.

In particular, profile P6 well illustrates the persistence of the substantial stability of the beach–dune system in test area A, without any setback of the dune front and only slight morpho-topographic changes in the backshore; it is therefore consistent with its previous evolution.

Profile C4, on the other hand, well represents the overall evolution of test area B, which has been affected by progressive shoreline and dune front retreat, while the backshore width has remained relatively stable (Table 5), consistent with what we observed from 2001 onwards.
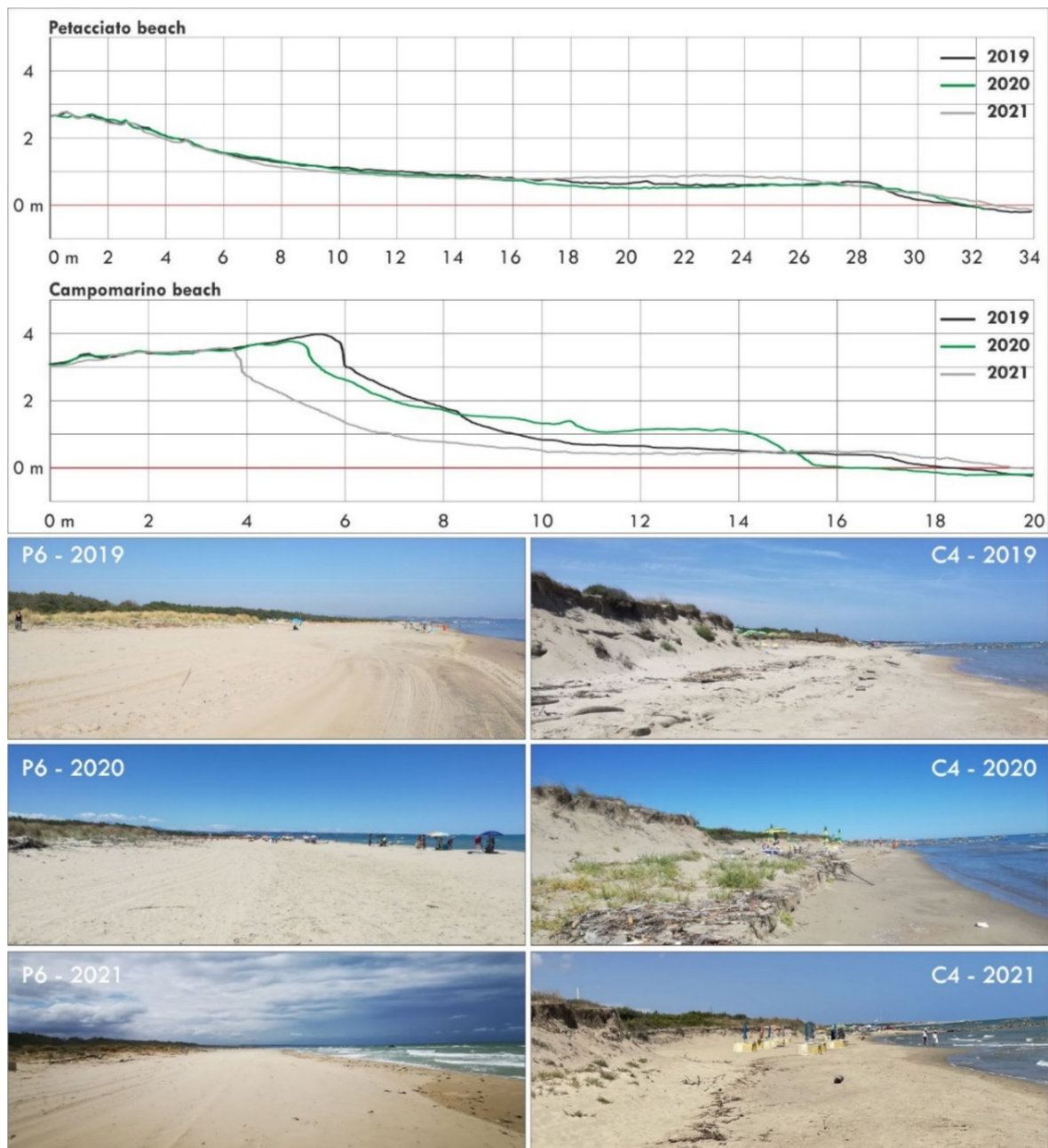
Figure 9. Representative beach profiles (C4 and P6) and panoramic views of test areas A and B.

4.3. Long- to Short-Term Shoreline Changes in the Test Areas and Related Erosion Indexes

The long- to short-term shoreline changes calculated for the beach profiles surveyed in the test areas, which were based on shoreline data referring to 1954, 2004, 2016, 2019, 2020, and 2021, provide the following data (Figure 10 and Tables 6 and 7).

Concerning the long-term evolution of test area A (the period of 1954–2016, Figure 10), the balance is clearly positive, as also evidenced by the average annual shoreline rates at around 1 m/y reconstructed for profiles P1–P7 (Table 6), and which is consistent with the evolution of S3 (Table 4). A minimum value of 1 has been attributed to the erosion indexes E_1 of profiles P1–P7.

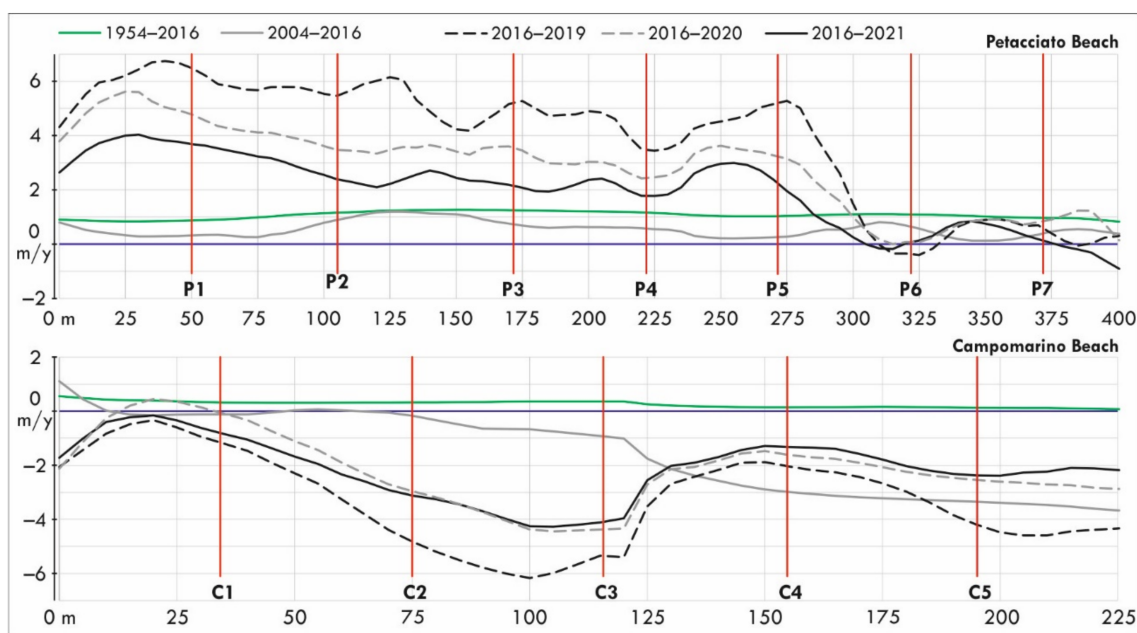**Figure 10.** Annual shoreline change rates calculated for the beach profiles surveyed in the study areas for the periods 1954–2016, 2004–2016, 2016–2019, 2016–2020, and 2016–2021.

Table 6. Shoreline changes in m (NSM) and annual shoreline change rates in m/y (LRR) calculated for the beach profiles in study areas A and B for the periods 1954–2016 and 2004–2016, and an evaluation of the related erosion indexes (E_1 and E_2).

Beach Profiles		1954–2016			2004–2016		
		NSM (m)	LRR (m/y)	E_1	NSM (m)	LRR (m/y)	E_2
Petacciato beach	P1	48.0	0.9	1	−3.3	−0.1	1
	P2	67.1	1.2	1	6.8	0.6	1
	P3	71.3	1.3	1	4.7	0.4	1
	P4	67.7	1.2	1	3.3	0.3	1
	P5	60.0	1.0	1	1.2	0.1	1
	P6	68.0	1.1	1	9.2	0.8	1
	P7	61.3	1.0	1	5.2	0.5	1
Campomarino beach	C1	11.0	0.3	1	−7.8	−0.7	2
	C2	15.0	0.3	1	−5.1	−0.4	1
	C3	18.1	0.4	1	−11.3	−1.0	2
	C4	0.4	0.1	1	−34.6	−3.1	4
	C5	−0.3	0.1	1	−37.7	−3.2	4

Regarding the long-term evolution of test area B (Figure 10), the obtained data document its substantial stability (C4-C5) as well as a slight trend to progradation (C1-C3), with the erosion indexes (E_1, Table 6) also assuming a minimum value of 1 in this case.

Considering then period of 2004–2016 (Figure 10), data show clear differences between the two test areas. The Petacciato area continues to exhibit a substantial stability, with all profiles being characterized by an erosion index of 1 (E_2, Table 6). The Campomarino area (C1–C5), however, is characterized by erosion indexes ranging from 1 to the maximum value of 4 (E_2, Table 6), highlighting its general destabilization and a significant trend toward erosion in the southern sector of B (C4–C5). These data are in agreement with those previously illustrated (Section 4.1, Figure 3) with regard to the stability conditions of segment S3 and the negative shoreline trend of the northernmost portion of segment S9 during the period of 2004–2016.

Table 7. NSM and LLR values calculated for profiles P1–P7 and C1–C5 for the periods 2016–2019, 2016–2020, and 2016–2021; related erosion indexes E_{2019}, E_{2020}, and E_{2021}; absolute shoreline variations (Net Shoreline Measurement) for the period of 2019–2021 (NSM 2019–2021).

Beach Profiles		2016–2019			2016–2020			2016–2021			2019–2021
		NSM (m)	LRR (m/y)	E_{2019}	NSM (m)	LRR (m/y)	E_{2020}	NSM (m)	LRR (m/y)	E_{2021}	NSM (m)
Petacciato beach	P1	22.8	6.5	1	18.9	4.8	1	18.5	3.7	1	−4.3
	P2	19.2	5.5	1	12.5	3.5	1	11.6	2.4	1	−7.6
	P3	16.9	4.8	1	14.3	3.6	1	9.7	2.3	1	−7.2
	P4	14.0	4.0	1	9.7	2.6	1	10.1	2.0	1	−3.9
	P5	17.7	5.0	1	12.7	3.4	1	14.2	2.7	1	−3.5
	P6	−1.2	−0.4	1	0.6	0.1	1	−1.7	−0.2	1	−0.5
	P7	2.3	0.7	1	3.4	0.7	1	0.7	0.3	1	−1.6
Campomarino beach	C1	−4.2	−1.2	3	1.4	−0.1	1	−7.3	−0.8	2	−3.1
	C2	−16.9	−4.8	4	−10.4	−3.0	4	−18.8	−3.1	4	−1.9
	C3	−18.8	−5.3	4	−18.2	−4.4	4	−22.6	−4.1	4	−3.8
	C4	−7.2	−2.0	4	−6.6	−1.6	3	−6.8	−1.3	3	0,4
	C5	−14.7	−4.2	4	−8.9	−2.5	4	−13.7	−2.4	4	1.0

Regarding the period of 2016–2021 (Table 7), our data for test area A confirm conditions of substantial stability as well as a slight trend toward shoreline progradation; for test area B, however, there is a slight to moderate trend toward shoreline retreat (Figure 10 and Table 7).

Considering the periods 2016–2019, 2016–2020, and 2019–2021 in detail, data obtained for test area A (Table 7) show that 2016–2019 was the most positive period, while the last three years (period 2019–2021) were characterized by a slight negative shoreline trend, with values between −0.5 m (P6) and −7.6 (P2) (NSM, Table 7). This negative shoreline trend, however, did not have any influence on the erosion index levels for profiles P1–P7, which remained equal to 1.

Conversely, the data calculated for test area B for the period of 2016–2019 (Table 7) show that this period was the most negative one, as it was characterized overall by the worst values for annual shoreline retreat rates (LRR up to −5.3 m/y, see C3) and by prevalent erosion indexes of 3 and 4 (E_{2019}, Table 7). Some amelioration in time is evidenced by profiles C1 and C4, whose erosion indexes decreased from 3 and 4 to 2 and 3, respectively, when considering the general period of 2016–2021 (Table 7).

Overall, these data highlight opposite trends for the two test areas. A slight trend toward destabilization for A, but without any effect on erosion indexes E_{2021}; a slight trend toward recovery for B, with some positive influence on erosion indexes E_{2021}. These trends appear to be clearly related to the increase of erosion along A and the decrease of erosion along B (see NSM values, Table 7) during the most recent period of 2019–2021.

4.4. Coastal Vulnerability Assessment

For the Coastal Vulnerability Assessment (CVA) of the test areas, the following three indexes were considered: the wave run-up height index I_{RU}, the short-term erosion index I_R (Tables 6 and 7), and the beach erosion index E, which were calculated using Formulas (2), (3), and (4), respectively.

4.4.1. The Wave Run-Up Height Index I_{RU}

$I_{RU2\%}$ levels were obtained by calculating the run-up values $R_{u2\%}$ and the related parameters $X_{Ru2\%}$ and $X_{Ru2\%}/L$ (width of the beach affected by run-up and relative percentage) for the beach profiles P1–P7 and C1–C5 for years 2019, 2020, and 2021 (Tables 8 and 9). Both normal wave ($H_s = 0.7$ m) and average extreme wave conditions ($H_t = 3.5$ m) were considered.

Table 8. Estimated run-up index values $I_{Ru2\%}$ and related parameters $X_{Ru2\%}$ and $X_{Ru2\%}/L$ under normal wave (Hs = 0.7 m) and average extreme wave conditions (H_t = 3.5 m).

		Petacciato Beach							Campomarino Beach				
		P1	P2	P3	P4	P5	P6	P7	C1	C2	C3	C4	C5
2019 H_s = 0.7 m	$X_{Ru2\%}$ (m)	4.1	2.9	3	3.1	3.6	3.1	3.2	3.5	3.3	3.4	3.1	5.3
	$X_{Ru2\%}/L$ (%)	12.0	10.2	10.7	11.0	15.0	13.6	16.9	33.5	35.9	14.0	45.9	109.1
	$I_{Ru2\%}$	1	1	1	1	1	1	1	1	2	1	2	4
2019 H_t = 3.5 m	$X_{Ru2\%}$ (m)	17.3	12.4	12.6	13.3	15.2	12.9	13.4	14.8	13.9	14.2	13.2	22.5
	$X_{Ru2\%}/L$ (%)	50.7	43.0	45.0	46.5	63.4	57.2	71.1	141.1	151.4	59.0	193.5	459.9
	$I_{Ru2\%}$	2	2	2	2	3	2	3	4	4	2	4	4
2020 H_s = 0.7 m	$X_{Ru2\%}$ (m)	3.2	3.1	3.2	3	3.4	3	3	3.2	3.1	3.1	2.9	3.3
	$X_{Ru2\%}/L$ (%)	18.0	15.9	13.2	12.7	19.1	19.8	19.6	27.1	31.6	12	48.4	36.2
	$I_{Ru2\%}$	1	1	1	1	1	1	1	1	1	1	2	1
2020 H_t = 3.5 m	$X_{Ru2\%}$ (m)	13.3	13.1	13.4	12.5	14.2	12.5	12.8	13.6	13.2	12.9	12.3	13.8
	$X_{Ru2\%}/L$ (%)	42.8	66.3	55.6	53.5	80.4	83.5	82.8	114.4	133.3	50.8	204.1	152.8
	$I_{Ru2\%}$	3	3	2	2	4	4	4	4	4	2	4	4
2021 H_s = 0.7 m	$X_{Ru2\%}$ (m)	4	3.5	3.3	3.4	3.9	3.5	3.8	3	3.4	4.2	4.2	3.4
	$X_{Ru2\%}/L$ (%)	13.1	16.2	16.2	13.8	19.0	16.5	23.1	36.2	44.9	21.2	69.5	56.7
	$I_{Ru2\%}$	1	1	1	1	1	1	1	1	2	1	3	2
2021 H_t = 3.5 m	$X_{Ru2\%}$ (m)	16.9	14.9	14	14.2	16.5	14.8	16.1	12.8	14.2	17.9	17.9	14.1
	$X_{Ru2\%}/L$ (%)	55.0	68.1	68.4	53.8	80.2	69.7	97.3	152.5	189.1	89.4	293.2	239.3
	$I_{Ru2\%}$	2	3	3	2	4	3	4	4	4	4	4	4

Table 9. Evaluation of short-term erosion indexes I_R for profiles P1–P7 and C1–C5, based on R values calculated for normal wave (H_s = 0.7 m) and average extreme wave conditions (H_t = 3.5 m), respectively.

		Petacciato Beach							Campomarino Beach				
		P1	P2	P3	P4	P5	P6	P7	C1	C2	C3	C4	C5
2019 H_s = 0.7 m	R (m)	2.9	0.1	0.2	1.0	0.1	1.9	0.26	2.0	3.3	0.1	3.1	3.7
	R/L (%)	8.6	0.5	0.8	3.4	0.1	8.4	1.4	19.4	29.6	0.6	45.4	74.7
	I_R	1	1	1	1	1	1	1	2	3	1	3	4
2019 H_t = 3.5 m	R (m)	5.2	6.3	6.7	9.3	7.4	11.0	8.8	12.4	13.7	7.0	14.1	15.8
	R/L (%)	15.1	22.0	24.0	32.5	30.9	48.9	44.1	118.2	148.6	29.1	207.7	321.5
	I_R	1	3	2	3	3	3	3	4	4	2	4	4
2020 H_s = 0.7 m	R (m)	0.7	0.6	1.2	1.9	2.4	2.2	1.5	2.8	1.1	0.1	3.3	3.7
	R/L (%)	2.3	2.8	5.9	7.4	10.0	12.2	8.8	23.8	11.0	0.5	54.7	74.7
	I_R	1	1	1	1	1	1	1	2	1	1	4	4
2020 H_t = 3.5 m	R (m)	8.9	8.9	10.7	11.5	12.3	11.2	10.1	12.9	9.7	8.2	13.6	14.8
	R/L (%)	28.7	44.8	48.9	44.6	50.6	61.6	59.0	108.6	98.2	32.6	227.0	164.6
	I_R	2	3	3	3	4	4	4	4	4	3	4	4
2021 H_s = 0.7 m	R (m)	15.9	5.5	0.2	0.1	0.1	0.1	0.2	8.9	5.3	0.2	3.4	1.3
	R/L (%)	51.7	24.9	1.0	0.1	0.1	0.5	1.0	106.1	70.2	0.9	57.0	22.8
	I_R	4	2	1	1	1	1	1	4	4	1	4	2
2021 H_t = 3.5 m	R (m)	1.0	3.5	5.7	6.9	8.5	8.6	9.3	20.3	16.7	6.4	14.6	11.4
	R/L (%)	3.2	15.8	27.8	28.1	41.7	40.6	56.4	241.9	222.2	31.9	239.4	192.4
	I_R	1	2	2	2	3	3	4	4	4	3	4	4

Regarding test area A, the results highlight the stable run-up height conditions under normal wave conditions (H_s = 0.7 m) from 2019 to 2021, with indexes $I_{Ru2\%}$ maintaining a minimum value of 1 for all profiles.

However, with regard to mean extreme wave conditions (H_t = 3.5 m), $I_{RU2\%}$ levels reached values between 2 and 3 in 2019 (P5 and P7, Table 8). In 2020, several negative variations in the $I_{RU2\%}$ levels were registered in the northern (P1–P2) and especially in the southern part (P5–P7) of the test area, where maximum values of 4 were calculated. Then, in 2021, both negative and positive variations were registered for parts of the profiles, resulting in final values between 2 and 4, and a condition substantially similar to that in 2020.

Regarding test area B, data highlight overall higher $I_{RU2\%}$ values under normal wave conditions (Table 8) for 2019 when compared with test area A, as well as several positive and negative variations in the $I_{RU2\%}$ values from 2019 to 2021, oscillating between 1 and 4. These variations, however, do not suggest any persisting positive or negative trend. Worthy of mention is the $I_{RU2\%}$ value of C3, which remained equal to 1 during all the three years.

When considering the average extreme wave conditions, all profiles were characterized by a maximum $I_{RU2\%}$ value of 4 in 2020 and 2021, except for C3 ($I_{RU2\%}$ value of 2, Table 8). This result highlights the generally worse run-up conditions of this beach during average extreme wave conditions, which can be generally related to the scarce width of the backshore. This is not the case for C3, i.e., the central portion of test area B, where the backshore is significantly wider and undergoes only a slight restriction from 2019 to 2021 (from 24.1 m to 20.0 m, Table 4). In this case, the increase of the run-up index value to 4 can be related to the decrease of the foreshore slope (from 10% to 5.3%, Table 5). In fact, as illustrated in Section 4.2, this portion of the beach has undergone important human interventions, resulting in enlargements, levelling, and the overall topographic lowering of the beach. Therefore, in our opinion, the worsening of the run-up conditions along C3 in 2021 is most likely related to these human interventions, showing that the latter did not contribute to the maintenance of the beach but, conversely, contributed to its major vulnerability to erosion.

4.4.2. The Short-Term Erosion Index I_R

Short-term erosion indexes I_{R2019}, I_{R2020}, and I_{R2021} were evaluated for both test areas (Petacciato beach, profiles P1–P7, and Campomarino beach, profiles C1–C5, Table 9) on the basis of R and R/L values obtained for both normal wave conditions (H_s = 0.7 m) and average extreme wave conditions (H_t = 3.5 m).

With regard to normal wave conditions, the results obtained for test area A highlight the persistence of low short-term erosion indexes (I_R values of 1, Table 9), with the only exception of the I_R2021 values for profiles P1 and P2, which increased to 4 and 2, respectively. However, regarding average extreme wave conditions, the profiles showed a notable variation in I_R values that oscillated between 1 and 4, but without showing any clear trend from 2019 to 2021.

The results obtained for test area B for normal wave conditions indicate a major variability of the short-term erosion indexes, which oscillated between values of 1 and 4, showing an overall worsening of erosion conditions from 2019 to 2021. The only exception is profile C3, which maintained an I_R value of 1, thus confirming the important role played by human interventions that have annually affected this portion of the beach. Concerning average extreme wave conditions, the I_R values reached maximum values of 4 for all profiles, with the only exception of C3, which is characterized by I_R values of 2 in 2019 and 3 in the following years, 2020 and 2021 (Table 9).

4.4.3. Variations in the CVA Parameters

The variations in the E, I_{RU}, and I_R indexes from 2019 to 2021 (Tables 7–9, for I_{RU} and I_R values, average extreme wave conditions were considered) led to significant variations in the related CVA levels, which were calculated according to Formula 1 (see Section 3.3).

In the case of test area A (Figure 11), with regard to data for 2019 and 2021, some profiles show the shift from low to medium CVA levels (P1, P3) or vice versa (P4); however, the other profiles show an overall slight increase of CVA values while remaining within the

medium level. These data give evidence of an overall slight increase of erosion susceptibility along the Petacciato beach. Furthermore, CVA values obtained for profiles P5, P6, and P7 for 2020 are even higher than those of 2021, indicating a temporary major worsening of CVA conditions for the southern portion of study area A from 2019 to 2020, which then partially recovered in 2021.
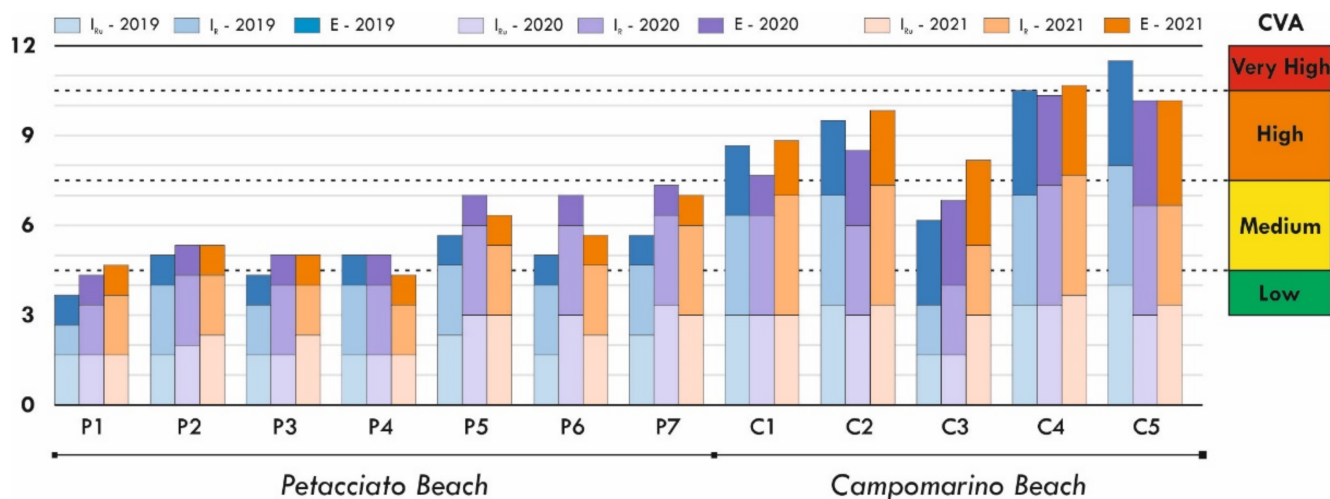

Figure 11. Comparison of I_{RU}, I_R, and E indexes and related CVA levels obtained respectively for 2019, 2020, and 2021 for the beach profiles surveyed in test areas A and B (Petacciato and Campomarino beaches).

Test area B, however, started 2019 with CVA values at the medium up to the very high CVA level, decidedly higher with respect to those of test area A. A comparison of 2019 and 2021 highlights very modest changes in the CVA values for C1, C2, and C4, the shift of C3 from a medium to a high CVA level, and that of C5 from a very high to a high CVA level. The CVA levels of 2020 are lower with respect to those of 2021, with the only exception of C5, where no change occurs from 2020 to 2021. Overall, only profile C3 shows a significant change in CVA values from 2019 to 2021, which can be mainly attributed to the negative variations, first in I_R and then in I_{RU} values (see also Tables 8 and 9). This profile has undergone, among all, the most significant negative changes in CVA values and the consequent increase of coastal vulnerability, which must be related, in our opinion, to the impact of human interventions in the central portion of test area B, which have been already reported and discussed before.

5. Discussion and Conclusions

The present study confirms that the Molise coast has been affected by severe shoreline erosion in the long-term period (1954–2016), which mainly affected the coastal segments that include the Trigno and Biferno river mouths (S1 and S7, Table 4).

A comparison of the most up-to-date previous shoreline change data for the period of 1954–2014 [21] with those obtained in this study for 1954–2016 shows that annual retreat rates in coastal segments S1 and S7 have slightly decreased from 2.7 m/y to 2.2 m/y and from 2.9 m/y to 2.7 m/y, respectively.

Concerning the mid-term shoreline evolution of the Molise coast (for the periods 2004–2014 [21] and 2004–2016 in this study), the comparisons highlight that erosion has increasingly affected S2 (−0.7 m/y in [21], −1.2 m/y in this study) and has also begun to affect S9 (0.5 m/y in [21], −0.5 m/y in this study), thus evidencing a slight strengthening of the erosion trend.

Regarding specifically the mid-term shoreline changes in test areas A and B (for the period of 2004–2016, Figure 10 and Table 6), the data highlight their stability and slight trend toward erosion, which are in line with the mid-term shoreline evolution of the coastal segments S3 and S9 (Table 4), which include them.

Finally, concerning the period of 2016–2021 (Table 7), the acquired data show that test area A prograded overall. However, morpho-topographical features and shoreline positions measured along profiles P1–P7 give evidence of a slight trend toward shoreline retreat from 2019 to 2021, although without any effect on the overall positive balance. Test area B, however, has already been affected by shoreline retreat and dune erosion at least since 2004 (Table 6), and it continued to be affected by erosion until 2021 (Table 7), resulting in a progressive degradation of the beach–dune system.

Changing beach and shoreline conditions in the test areas from 2019 to 2021 has induced several changes in the values of the parameters used in the CVA assessment, and therefore changes in the resulting CVA values/levels. The CVA values obtained for 2019 and 2021 highlight a general although modest trend towards increasing coastal vulnerability for both test areas. In detail, the most significant negative changes in CVA values concern profile C3, pointing out the negative effect of human interventions on the coastal vulnerability of the central portion of test area B.

The obtained results highlight, according to other studies realized in similar coastal contexts [44–46], that beach–dune systems can undergo significant changes in the short-term period and even from one year to the next, thus becoming part of a persisting trend or simply presenting as evidence of reversible fluctuations. Consequently, short-term/annual monitoring of shoreline dynamics and morphometric changes in the beach–dune system appears to be essential in order to detect in time and supervise erosion trends.

Moreover, the integration of traditional investigation methods—mainly those based on available photogrammetric and/or satellite imagery and GPS measurements—with the more innovative UAV survey technology allows for an increase of the scale of observation and monitoring as well as for the detection and updating of the most recent beach–dune and shoreline changes in an efficient, cheaper, and rapid way.

The demonstration that shoreline and beach morphology changes from 2019 to 2021 have caused variations in the indexes that enter in the CVA assessment highlights the need for and the opportunity to update such indexes in a rapid and efficient manner by using the proposed UAV approach, especially in critical erosion hotspot areas under monitoring.

In conclusion, the relatively simple use of UAV technology, along with the possibility to acquire DEMs and georeferenced images with high spatio-temporal resolution, allow this technology to excellently lend itself to the integration of existing coastal change and shoreline migration mapping methodologies and databases. Moreover, the integrated use of UAV and GIS approaches has proven to be an effective instrument, not only for a quick spatial data analysis, but also in order to offer an objective approach with consistent measurement and calculation processes.

References

1. Spencer, T.; French, J.R. Coastal processes and landforms. *Geol. Soc. Lond. Mem.* **2022**, *58*, M58-2021-2034. [CrossRef]
2. Masselink, G.; Hughes, M.; Knight, J. *Introduction to Coastal Processes & Geomorphology*, 2nd ed.; Routledge: Oxfordshire, UK, 2011.
3. Short, A.; Jackson, D. *Beach Morphodynamics*, 2nd ed.; Elsevier: Amsterdam, The Netherlands, 2020.

4. Nicholls, R.; Wong, P.; Burket, V.; Codignotto, J.; Hay, J.; McLean, R.; Ragoonaden, S.; Woodroffe, C. Coastal systems and low-lying areas. In *Climate Change 2007: Impacts, Adaptation and Vulnerability, Contribution of Working Group II to the Fourth Assessment Report of the Intergovernmental Panel on Climate Change*; Parry, M.L., Canziani, O.F., Palutikof, J.P., Van der Linden, P.J., Hanson, C.E., Eds.; Cambridge University Press: Cambridge, UK, 2007; pp. 315–356.

5. Woodroffe, C. *The Natural Resilience of Coastal Systems: Primary Concepts*; University of Wollongong: Wollongong, NSW, Australia, 2007.

6. He, Y.; Wu, Y.; Lu, C.; Wu, M.; Chen, Y.; Yang, Y. Morphological change of the mouth bar in relation to natural and anthropogenic interferences. *Cont. Shelf Res.* **2019**, *175*, 42–52. [CrossRef]

7. Zimmermann, M.; Erikson, L.H.; Gibbs, A.E.; Prescott, M.M.; Escarzaga, S.M.; Tweedie, C.E.; Kasper, J.L.; Duvoy, P.X. Nearshore bathymetric changes along the Alaska Beaufort Sea coast and possible physical drivers. *Cont. Shelf Res.* **2022**, *242*, 104745. [CrossRef]

8. Valentine, K.; Mariotti, G. Wind-driven water level fluctuations drive marsh edge erosion variability in microtidal coastal bays. *Cont. Shelf Res.* **2019**, *176*, 76–89. [CrossRef]

9. Pirazzoli, P.A.; Tomasin, A. Recent near-surface wind changes in the central Mediterranean and Adriatic areas. *Int. J. Climatol.* **2003**, *23*, 963–973. [CrossRef]

10. Buccino, M.; Paola, G.D.; Ciccaglione, M.C.; Giudice, G.D.; Rosskopf, C.M. A medium-term study of molise coast evolution based on the one-line equation and "equivalent wave" concept. *Water* **2020**, *12*, 2831. [CrossRef]

11. UN. The Ocean Conference. *Factsheet: People and Oceans. New York 2017.* Available online: https://www.un.org/sustainabledevelopment/wp-content/uploads/2017/05/Ocean-fact-sheet-package.pdf (accessed on 1 February 2022).

12. Nicholls, R.J.; Marinova, N.; Lowe, J.A.; Brown, S.; Vellinga, P.; De Gusmão, D.; Hinkel, J.; Tol, R.S.J. Sea-level rise and its possible impacts given a 'beyond 4 °C world' in the twenty-first century. *Philos. Trans. R. Soc. A* **2011**, *369*, 161–181. [CrossRef]

13. MATTM. National Macro Data on the Coast Line Changes from 1960 to 2012. Available online: http://www.pcn.minambiente.it/mattm/en/project-coasts/ (accessed on 1 February 2022).

14. Minervino Amodio, A.; Di Paola, G.; Rosskopf, C.M. Monitoring Coastal Vulnerability by Using DEMs Based on UAV Spatial Data. *ISPRS Int. J. Geo-Inf.* **2022**, *11*, 155. [CrossRef]

15. Gioia, D.; Amodio, A.M.; Maggio, A.; Sabia, C.A. Impact of land use changes on the erosion processes of a degraded rural landscape: An analysis based on high-resolution DEMs, historical images, and soil erosion models. *Land* **2021**, *10*, 673. [CrossRef]

16. Flores-de-Santiago, F.; Valderrama-Landeros, L.; Rodríguez-Sobreyra, R.; Flores-Verdugo, F. Assessing the effect of flight altitude and overlap on orthoimage generation for UAV estimates of coastal wetlands. *J. Coast. Conserv.* **2020**, *24*, 1–11. [CrossRef]

17. Colomina, I.; Molina, P. Unmanned aerial systems for photogrammetry and remote sensing: A review. *ISPRS J. Photogramm. Remote Sens.* **2014**, *92*, 79–97. [CrossRef]

18. Nield, J.M.; Wiggs, G.F.; Squirrell, R.S. Aeolian sand strip mobility and protodune development on a drying beach: Examining surface moisture and surface roughness patterns measured by terrestrial laser scanning. *Earth Surf. Processes Landf.* **2011**, *36*, 513–522. [CrossRef]

19. Coveney, S.; Stewart Fotheringham, A.; Charlton, M.; McCarthy, T. Dual-scale validation of a medium-resolution coastal DEM with terrestrial LiDAR DSM and GPS. *Comput. Geosci.* **2010**, *36*, 489–499. [CrossRef]

20. Aucelli, P.P.C.; Iannantuono, E.; Rosskopf, C.M. Recent evolution and erosion risk of the Molise coast (southern Italy). *Boll. Della Soc. Geol. Ital.* **2009**, *128*, 759–771. [CrossRef]

21. Rosskopf, C.M.; Di Paola, G.; Atkinson, D.E.; Rodríguez, G.; Walker, I.J. Recent shoreline evolution and beach erosion along the central Adriatic coast of Italy: The case of Molise region. *J. Coast. Conserv.* **2018**, *22*, 879–895. [CrossRef]

22. Aucelli, P.P.C.; Di Paola, G.; Rizzo, A.; Rosskopf, C.M. Present day and future scenarios of coastal erosion and flooding processes along the Italian Adriatic coast: The case of Molise region. *Environ. Earth Sci.* **2018**, *77*, 1–19. [CrossRef]

23. Bracone, V.; Amorosi, A.; Aucelli, P.P.C.; Rosskopf, C.M.; Scarciglia, F.; Di Donato, V.; Esposito, P. The Pleistocene tectono-sedimentary evolution of the Apenninic foreland basin between Trigno and Fortore rivers (Southern Italy) through a sequence-stratigraphic perspective. *Basin Res.* **2012**, *24*, 213–233. [CrossRef]

24. Berardo, F.; Carranza, M.L.; Frate, L.; Stanisci, A.; Loy, A. Seasonal habitat preference by the flagship species Testudo hermanni: Implications for the conservation of coastal dunes. *Comptes Rendus-Biol.* **2015**, *338*, 343–350. [CrossRef]

25. Stanisci, A.; Acosta, A.; Carranza, M.L.; Feola, S.; Giuliano, M. Habitats of European Community Interest along Molise coast and their naturalistic value based on flora. *Fitosociologia* **2007**, *44*, 171–175.

26. Cavaleri, L.; Bertotti, L.; Tescaro, N. The modelled wind climatology of the Adriatic Sea. *Theor. Appl. Climatol.* **1997**, *56*, 231–254. [CrossRef]

27. Signell, R.P.; Carniel, S.; Cavaleri, L.; Chiggiato, J.; Doyle, J.D.; Pullen, J.; Sclavo, M. Assessment of wind quality for oceanographic modelling in semi-enclosed basins. *J. Mar. Syst.* **2005**, *53*, 217–233. [CrossRef]

28. Bonaldo, D.; Bucchignani, E.; Ricchi, A.; Carniel, S. Wind storminess in the adriatic sea in a climate change scenario. *Acta Adriat.* **2017**, *58*, 195–208. [CrossRef]

29. Parea, G.C. Trasporto dei Sedimento ed Erosione Costiera Lungo il Litorale fra il Tronto ed il Fortore (Adriatico Centrale). 1978, pp. 361–367. Available online: https://discovery.sba.uniroma3.it/primo-explore/fulldisplay/39cab_almap2156010230002653/ (accessed on 15 July 2022).

30. Aucelli, P.P.C.; De Pippo, T.; Iannantuono, E.; Rosskopf, C.M. Caratterizzazione morfologico-dinamica e meteomarina della costa molisana nel settore compreso tra la foce del torrente Sinarca e Campomarino Lido (Italia meridionale). *Studi Costieri* **2007**, 75–92.

31. Lionello, P.; Barriopedro, D.; Ferrarin, C.; Nicholls, R.J.; Orlić, M.; Raicich, F.; Reale, M.; Umgiesser, G.; Vousdoukas, M.; Zanchettin, D. Extreme floods of Venice: Characteristics, dynamics, past and future evolution (review article). *Nat. Hazards Earth Syst. Sci.* **2021**, *21*, 2705–2731. [CrossRef]

32. ISPRA. Stazioni mariografiche—Ortona. 2022. Available online: https://www.mareografico.it/?session=0S382360463875O7087KIA65&syslng=ita&sysmen=-1&sysind=-1&syssub=-1&sysfnt=0&code=STAZ&idst=17&idreq=1@1@2&set=date (accessed on 1 February 2022).

33. Martínez Del Pozo, J.Á.; Anfuso, G. Spatial approach to medium-term coastal evolution in south Sicily (Italy): Implications for coastal erosion management. *J. Coast. Res.* **2008**, *24*, 33–42. [CrossRef]

34. Himmelstoss, E.A.; Henderson, R.E.; Kratzmann, M.G.; Farris, A.S. *Digital Shoreline Analysis System (DSAS) Version 5.0 User Guide*; 2018-1179; US Geological Survey: Reston, VA, USA, 2018.

35. Eltner, A.; Baumgart, P.; Maas, H.G.; Faust, D. Multi-temporal UAV data for automatic measurement of rill and interrill erosion on loess soil. *Earth Surf. Processes Landf.* **2015**, *40*, 741–755. [CrossRef]

36. Snavely, N.; Seitz, S.M.; Szeliski, R. Modeling the world from Internet photo collections. *Int. J. Comput. Vis.* **2008**, *80*, 189–210. [CrossRef]

37. Di Paola, G.; Aucelli, P.P.C.; Benassai, G.; Rodríguez, G. Coastal vulnerability to wave storms of Sele littoral plain (southern Italy). *Nat. Hazards* **2014**, *71*, 1795–1819. [CrossRef]

38. Anfuso, G.; Postacchini, M.; Di Luccio, D.; Benassai, G. Coastal sensitivity/vulnerability characterization and adaptation strategies: A review. *J. Mar. Sci. Eng.* **2021**, *9*, 72. [CrossRef]

39. Di Paola, G.; Aucelli, P.P.C.; Benassai, G.; Iglesias, J.; Rodríguez, G.; Rosskopf, C.M. The assessment of the coastal vulnerability and exposure degree of Gran Canaria Island (Spain) with a focus on the coastal risk of Las Canteras Beach in Las Palmas de Gran Canaria. *J. Coast. Conserv.* **2018**, *22*, 1001–1015. [CrossRef]

40. Di Luccio, D.; Benassai, G.; Di Paola, G.; Rosskopf, C.M.; Mucerino, L.; Montella, R.; Contestabile, P. Monitoring and modelling coastal vulnerability and mitigation proposal for an archaeological site (Kaulonia, Southern Italy). *Sustainability* **2018**, *10*, 2017. [CrossRef]

41. Stockdon, H.F.; Holman, R.A.; Howd, P.A.; Sallenger, A.H., Jr. Empirical parameterization of setup, swash, and runup. *Coast. Eng.* **2006**, *53*, 573–588. [CrossRef]

42. Kriebel, D.L.; Dean, R.G. Convolution method for time-dependent beach-profile response. *J. Waterw. Port Coast. Ocean Eng.* **1993**, *119*, 204–226. [CrossRef]

43. Crowell, M.; Leatherman, S.P.; Buckley, M. Shoreline change rate analysis: Long term versus short term data. *Shore Beach* **1993**, *61*, 13–20.

44. Laporte-Fauret, Q.; Marieu, V.; Castelle, B.; Michalet, R.; Bujan, S.; Rosebery, D. Low-Cost UAV for high-resolution and large-scale coastal dune change monitoring using photogrammetry. *J. Mar. Sci. Eng.* **2019**, *7*, 63. [CrossRef]

45. Scarelli, F.M.; Sistilli, F.; Fabbri, S.; Cantelli, L.; Barboza, E.G.; Gabbianelli, G. Seasonal dune and beach monitoring using photogrammetry from UAV surveys to apply in the ICZM on the Ravenna coast (Emilia-Romagna, Italy). *Remote Sens. Appl. Soc. Environ.* **2017**, *7*, 27–39. [CrossRef]

46. Turner, I.L.; Harley, M.D.; Drummond, C.D. UAVs for coastal surveying. *Coast. Eng.* **2016**, *114*, 19–24. [CrossRef]